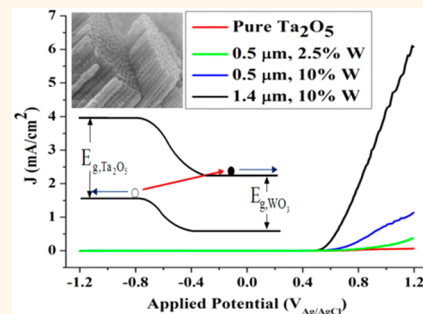


Self-Assembled Nanostructured Photoanodes with Staggered Bandgap for Efficient Solar Energy Conversion

Ramy Nashed,[†] Paul Szymanski,[‡] Mostafa A. El-Sayed,[‡] and Nageh K. Allam^{†,*}

[†]Energy Materials Lab (EML), School of Sciences and Engineering, The American University in Cairo, New Cairo 11835, Egypt and [‡]Laser Dynamics Lab (LDL), School of Chemistry and Biochemistry, Georgia Institute of Technology, Atlanta, Georgia 30332, United States

ABSTRACT Vertically oriented Ta–W–O nanotube array films were fabricated via the anodization of Ta–W alloy foils in HF-containing electrolytes. HF concentration is a key parameter in achieving well-adhered nanotube array structure. X-ray photoelectron spectroscopy (XPS) and diffuse reflectance measurements confirm the staggered band-alignment between Ta_2O_5 and WO_3 , which facilitates the separation of charge carriers. The nanotubes made of Ta–W films containing 10% W showed 100-fold improvement in the measured photocurrent compared to pristine Ta_2O_5 upon their use to split water photoelectrochemically. This enhancement was related to the efficient charge transport and the red shift in absorption spectrum with increase of the W content, which was asserted by ultrafast transient absorption (TA) spectroscopy measurements. The TA measurements showed the elimination of trap states upon annealing Ta–W–O nanotubes and, hence, minimizing the charge carrier trapping, whereas the trap states remain in pristine Ta_2O_5 nanotubes even after annealing.



KEYWORDS: Ta–W–O · staggered bandgap · solar · transient absorption · laser dynamics

The total energy needed to power the planet in a year is less than the sunlight energy reaching the earth in 1 h.¹ Therefore, the challenge facing modern society is the efficient use of the enormous solar energy resource rather than identifying a sustainable energy source. Among the various storage protocols considered in recent years, solar fuels² are of particular interest because they can be easily integrated with the existing fuel storage and delivery infrastructure.

Despite the significant amount of work over the past decades to design and develop new functional materials for the solar fuel production,^{3–8} the long-standing bottleneck is to achieve an efficient charge separation mechanism without compromising the bandgap. In fact, most of the proposed photoanodes to date suffer from high charge trapping problems, which limit their photoconversion efficiency. Toward this end, we have recently reported a detailed density functional theory (DFT) study on the Ta–W–O mixed oxide system.⁹ The Ta–W–O system experiences bandgap bowing with a highly tunable bandgap ranging

from 3.7 eV for pristine Ta_2O_5 down to 1 eV for 50% W content.⁹ Also, the calculations showed that Ta–W–O has very low hole effective mass, comparable to that of III–V materials.⁹

Herein, we demonstrate, for the first time, the opportunity to fabricate Ta–W–O mixed oxide nanotube arrays by a facile electrochemical method and investigate their performance as photoanodes in photoelectrochemical water splitting cells. The dynamics of charge carriers were also investigated to understand the reasons behind the enhanced performance of the fabricated nanotubes.

RESULTS AND DISCUSSION

Figure S1 (Supporting Information) shows the effect of anodization time, applied voltage, and HF concentration on the length, diameter, and wall thickness of the resulted nanotube arrays. Note that the wall thickness of the resulted nanotubes containing 10% W is smaller than their 2.5% W counterpart, which is expected to facilitate the diffusion of the photogenerated hole to the electrode/electrolyte interface, hence enhancing the water oxidation process.

* Address correspondence to nageh.allam@aucegypt.edu.

Received for review February 14, 2014 and accepted April 14, 2014.

Published online April 14, 2014
10.1021/nn5009066

© 2014 American Chemical Society

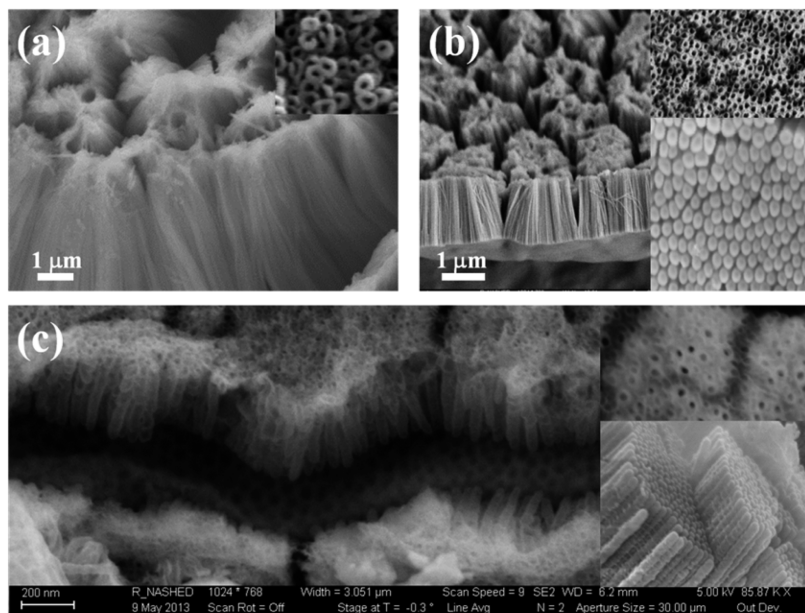


Figure 1. FESEM images of the films resulted upon the anodization of (a) pure Ta, (b) Ta-2.5% W, and (c) Ta-10% W foils at 15 V in 16.4 M H_2SO_4 and 2.9 M HF electrolytes for 3 min.

Note also that the anodization time has more pronounced effect on the 10% W alloy compared to the 2.5% W-containing alloy. For example, upon increasing the anodization time from 15 to 35 min, the nanotube length increases from 0.84 to 1.2 μm for the 2.5% W alloy, whereas it changes from 1.2 to 6.4 μm for the 10% W alloy. Increasing the anodization potential resulted in an increase in the nanotube length and diameter for both 2.5% and 10% W alloys, with a higher effect on the 10% W alloy (Figure S1c,d). The nanotube wall thickness increases from 9 to 20.5 nm for the 2.5% W alloy, whereas it nearly remains constant at around 10.5 nm for the 10% W alloy as the anodization potential increases from 10 to 20 V. Although the nanotube length for the 2.5% W alloy does not seem to be affected by the anodization time and applied potential, it is influenced by the HF concentration, where the nanotube length increases from 0.6 to 3.2 μm as the HF concentration increases from 0.51 to 0.85 M then it decreases to 1.2 μm at 1.17 M HF (Figure S1e). The nanotube diameter and wall thickness show the same dependence on HF concentration. Figure S2 in the Supporting Information shows the SEM images for the resulted nanotubes at different conditions.

Although we were able to fabricate nanotubes with controlled length, diameter, and wall thickness, they do not adhere well to the substrate upon their annealing, due to the formation of TaF_5 layer between the oxide layer and the alloy substrate.^{10,11} In an attempt to limit the formation of the TaF_5 barrier layer, the anodization was done in relatively short times. The anodization of Ta and Ta-W foils in an electrolyte containing 2.9 M HF and 16.4 M H_2SO_4 at 15 V resulted in the formation of well-adhered nanotube layers. It is

noteworthy that for pure Ta and 2.5% W alloy, we were able to fabricate nanotubes after 20 s only, whereas at least 2 min of anodization were needed for the Ta-10% W alloy in order to obtain nanotubular structure. This is probably due to the formed WO_3 , which has different reactivity toward F^- ions compared to Ta_2O_5 . This is asserted by the fact that the maximum obtained nanotube length decreases progressively from 3.3 μm for pure Ta_2O_5 to 2.1 μm for 2.5% W, to 1.4 μm for 10% W, with increasing the amount of W. Figure 1 shows the SEM images of the obtained nanotubes.

The fabricated nanotubes have an orthorhombic crystal structure with estimated volume expansions of 2.9% and 3.8% for the samples containing 2.5% W and 10% W, respectively compared to pristine Ta_2O_5 .⁹ Figure 2 shows the XRD pattern for pristine and Ta-W-O mixed oxide nanotubes that have been annealed at 450 °C for different annealing times. Generally, the peaks are shifted toward higher 2θ values as the annealing time increases, indicating a contraction in the crystal lattice. This is because heating the lattice for longer times allows the atoms to readjust their positions, minimizing the total energy of the system. The trend is not the same for the samples containing 10% W, where mainly intensity fluctuations and a slight shift to lower 2θ values occurred upon annealing. These samples appear to have phase separation with increased splitting of the higher 2θ peaks relative to the corresponding peaks of the 2.5% W-containing samples. Also, the extent of peak shifting decreases as the W content increases, which can be attributed to the fact that W atom has larger size than Ta atom, allowing less space for the atoms to move in the lattice, in turn decreasing

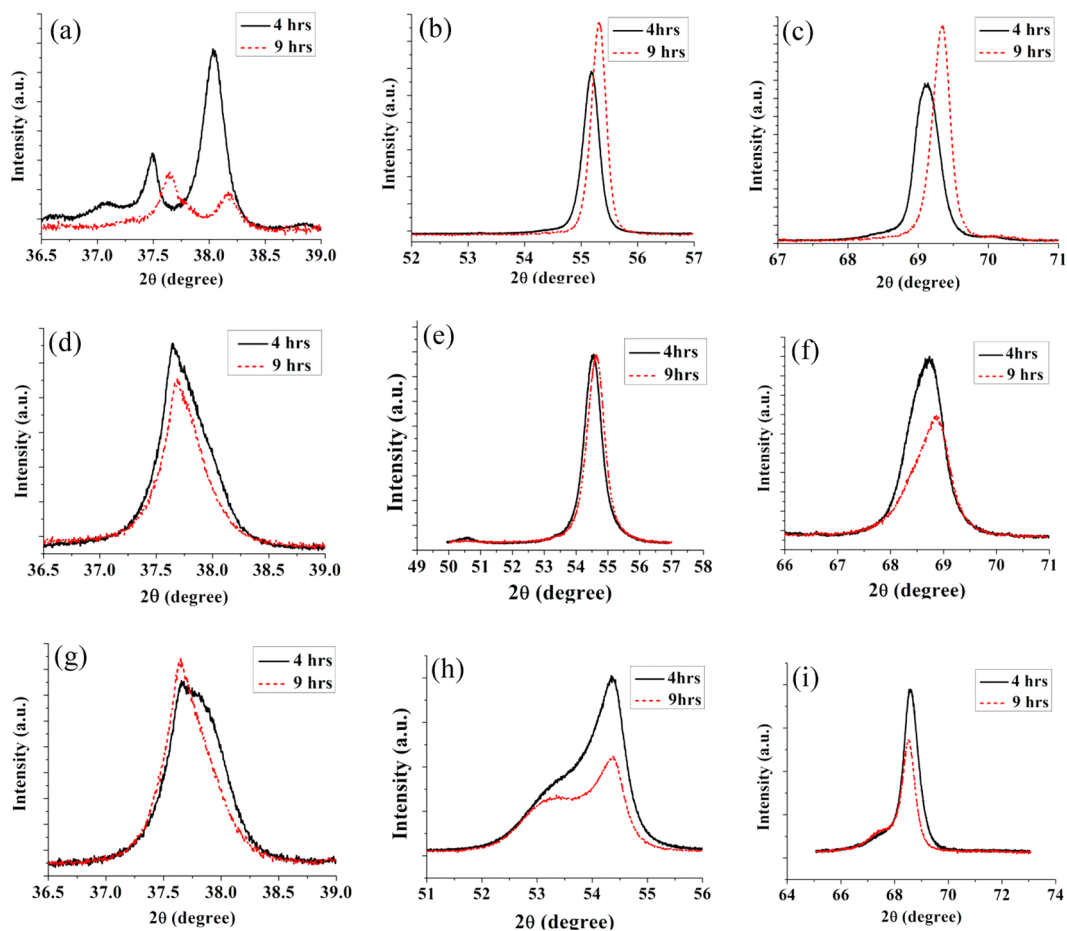


Figure 2. XRD pattern for the annealed (a–c) pristine, (d–f) Ta–2.5% W–O, and (g–i) Ta–10% W–O nanotube samples.

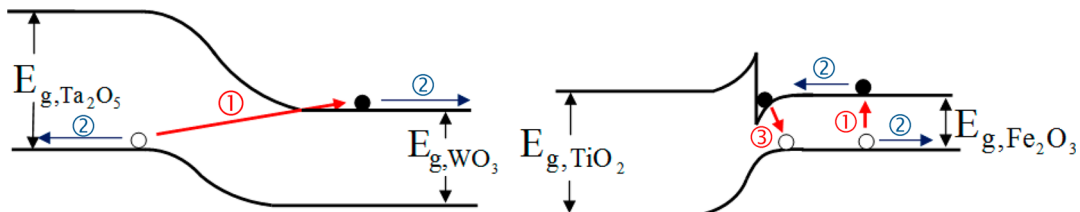


Figure 3. Energy band diagrams of (a) Ta–W–O and (b) Ti–Fe–O, showing the charge carrier transport for both systems, thus illustrating the efficient charge separation in Ta–W–O alloy.

the extent of freedom for readjustment. Note that the peak shoulder at $2\theta = 53^\circ$ (plane (331) in WO_3) indicates the presence of a small precipitation of WO_3 -rich phase leading to a microscale heterojunction. This helps in the charge separation, which in turn is expected to result in a higher electric current, since Ta_2O_5 – WO_3 heterojunction was found to have a staggered bandgap.⁹ Figure 3 illustrates the staggered bandgap alignment in Ta–W–O alloy. Upon illumination, the electrons are excited from the valence band of Ta_2O_5 to the conduction band of WO_3 . Electrons have a potential barrier toward the Ta_2O_5 side, which forces them to flow rightward, whereas holes have a potential barrier toward the WO_3 side forcing them to flow leftward, and hence an efficient charge separation is achieved.⁹ On the other hand, straddled

band alignment (such as that present in Ti–Fe–O system) gives rise to electron trapping in the conduction band, as shown in Figure 3b, and, in turn, reduces the conversion efficiency.^{9,12} We believe that this is the main reason behind the modest efficiency reported so far for photoelectrochemical water splitting systems based on straddled band alignment.

To study the composition of the fabricated Ta_2O_5 and Ta–W–O nanotubes, XPS analysis was performed, Figure 4. The O 1s peak was observed between 530.5 and 530.9 eV, in agreement with the O 1s peak reported for Ta_2O_5 and WO_3 .^{13–16} In pure Ta_2O_5 , Ta 4f peaks exist at 26.3 and 28.1 eV corresponding to $4f_{7/2}$ and $4f_{5/2}$ peaks, respectively, with a separation of 1.8 eV, indicating the existence of Ta^{5+} .¹⁷ As the W content increases

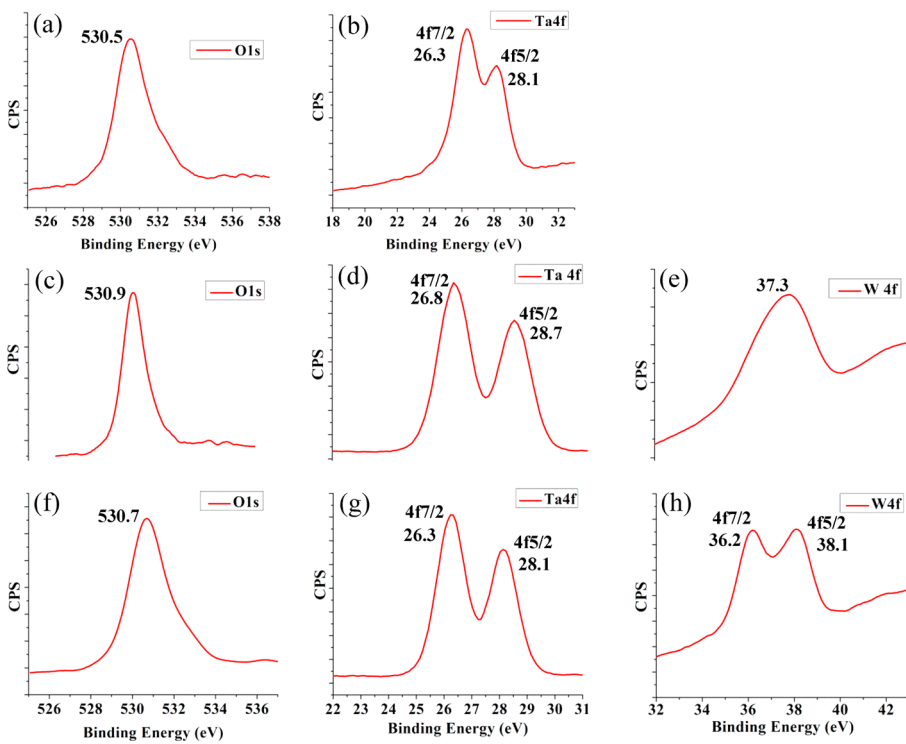


Figure 4. XPS analysis for (a and b) pure Ta_2O_5 , (c–e) 2.5% W, and (f–h) 10% W.

to 2.5%, both the O 1s peak and the Ta 4f peaks are shifted toward higher binding energies, indicating a decrease in the electron cloud around both oxygen and tantalum. This suggests an electron transfer from both O and Ta to W. The nominal peak separation of the W 4f is ~ 2.2 eV, which should be easily resolvable. The presence of a single W 4f peak for the sample containing 2.5% W indicates multiple oxidation states.¹⁸ Following the work of Khyzun,¹⁸ the coordination of W can be assigned to a suboxide with stoichiometry closer to WO_2 , making W a p-type dopant at these low concentrations. The acceptor levels generated by W would then allow electron density to be away from Ta and O, causing the observed shifts to higher binding energies. At 10% W content, the peak splits into the $4f_{7/2}$ and $4f_{5/2}$ levels (Figure 4h). From this observation and using Khyzun's earlier study,¹⁸ we were able to predict the stoichiometry of the WO_x (in the sample containing 10% W) to be $2.77 < x \leq 3$. This shift in the oxygen coordination of W reverses the initial increase in acceptor levels and consequently reverts the Ta and O core levels back to be close to that of the matrix Ta_2O_5 (Figure 4f, g).

Figure 5a shows the absorption spectrum of pure Ta_2O_5 as well as the Ta–W–O nanotube array films. As the W content increases, the absorption is red-shifted from that of pristine Ta_2O_5 , indicating a decrease in the bandgap of the W-containing samples. This reduction in the bandgap is due to lowering of the conduction band edge, as the conduction band of Ta_2O_5 (Ta 5d orbital^{19,20}) is higher in energy than that of W (W 5d).²¹

Furthermore, there is an absorption tail, which extends in the visible region as the W content increases. This can be understood from the Crystal Field Theory, where the W 5d orbitals are split into a set of filled orbitals occurring at a lower energy and another set of empty orbitals occurring at a higher energy. The splitting occurs when a set of negative point charges moves close to W atoms. The energy of some of the d-orbitals rises due to the repulsion between the d-orbital electrons and the electrons approaching the W^{4+} . Each d-orbital is affected differently depending on the geometry of the surrounding negative charges. This asserts our assumption that upon illumination, the electrons are excited from the VB of Ta_2O_5 to the CB of WO_3 .⁹ When the electrons are transferred toward WO_3 , they increase the charge density around the W atoms causing the splitting of the d-orbitals. Figure 5a asserts that the extended absorption is mainly due to splitting of W 5d orbital and not Ta 5d because the absorption tail gets more extended as the amount of W increases.

The photoelectrochemical activity of the fabricated nanotubes to split water was investigated. Figure 5b shows the variation of photocurrent density with applied potential for pure Ta_2O_5 and Ta–W–O nanotubes. The photocurrent increases monotonically as the W content increases (almost by 100-fold), which can be attributed to the red shift in the absorption spectrum upon adding W as well as the high carrier separation efficiency resulting from the staggered bandgap nature of Ta–W–O.⁹ Furthermore, with the knowledge that Ta–W–O system has an indirect

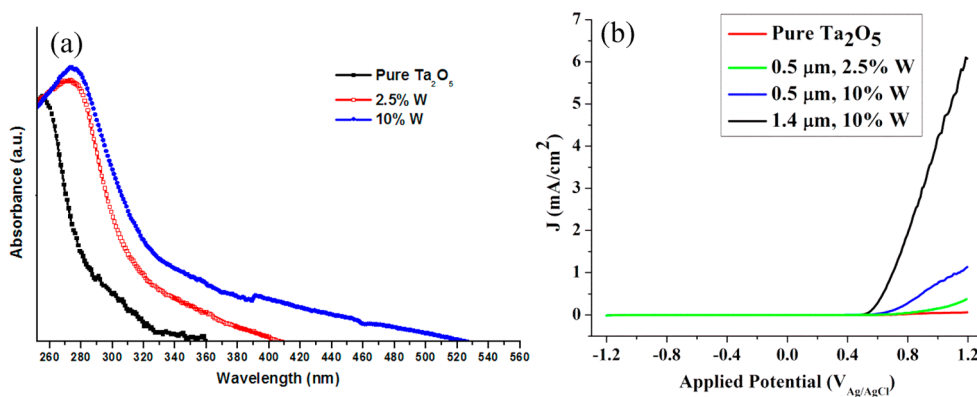


Figure 5. (a) Diffuse reflectance spectra (DRS) for pure Ta_2O_5 and $\text{Ta}-\text{W}-\text{O}$ nanotube electrodes annealed at 450 $^{\circ}\text{C}$ for 9 h in air; (b) photocurrent density versus potential in 1 M KOH solution under AM1.5 illumination for pure Ta_2O_5 and $\text{Ta}-\text{W}-\text{O}$ nanotubes.

bandgap,⁹ the length of the nanotubes is a significant factor in improving photon absorption, as indirect bandgap materials have low absorption coefficients compared to their direct bandgap counterparts,²² and hence, the optical path of light needs to be increased in order to increase the probability of photon absorption. This is asserted in Figure 5b where the photocurrent increases by more than five times with increasing the nanotube length in the sample containing 10% W from 0.5 to 1.4 μm . Moreover, the onset potential is shifted toward more negative values as the W content increases. This is because as the W content increases, the donor energy level is shifted more toward the conduction band edge, which in turn, shifts the Fermi level toward more negative potential. This is a desirable property since this open circuit potential represents the contribution of light toward the minimum potential difference required for water splitting (1.23 V).² Table S1 summarizes the obtained onset potentials as well as the maximum photocurrent density for Ta_2O_5 and $\text{Ta}-\text{W}-\text{O}$ nanotubes.

Transient absorption (TA) spectroscopy was shown to be a very efficient technique to investigate the charge carrier dynamics in semiconductor films.^{23–29} In fact, TA spectroscopy is playing a vital role in the advancement of dye-sensitized solar cells by providing a very deep understanding on charge carriers separation, transport, and recombination, which, in turn, allows for overcoming the deficiencies in the device performance and hence help designing more efficient systems for energy conversion.^{27–29} Unfortunately, the analogous process in photoelectrochemical conversion (PEC) is not yet understood to the same level of details as the solar cell counterpart. Therefore, a lot more work is still needed in this field to achieve adequately efficient PEC systems.³⁰

The TA spectra (Figures 6 and 7) and dynamics (Figure 8) were collected for the longest nanotube samples of each doping level at a pump energy of 800 nJ/pulse, the lowest energy where a measurable signal could be obtained for every sample. A Helios UV-visible

spectrometer (Ultrafast Systems) was used for the measurements. Two different pump wavelengths were used to compare UV (340 nm) with visible (490 nm) excitation. Pump light at 340 nm was obtained from the fourth harmonic of the signal from a Coherent OPerA Solo optical parametric amplifier, which was pumped by a Coherent Libra regeneratively amplified Ti:sapphire laser (809 nm, 50 fs pulses, 1 kHz repetition rate). The sum frequency of the signal and the laser fundamental wavelength was used to produce pump light at 490 nm. A broadband probe beam was produced by focusing a small fraction of the fundamental wavelength into a sapphire crystal. Both pump and probe were focused and overlapped on the surface of the substrate, with the pump spot diameter \sim 1 mm. As the metal substrates do not transmit light, reflected probe light is used to determine the transient absorption by focusing it into a fiber-coupled Si array detector with a detection range of 300–907 nm. Typically, only probe light at 700 nm and above could be collected in a reasonable amount. A chopper blocks every other pump pulse with the difference between two consecutive spectra, one with the pump beam and one without, yielding the TA signal $\Delta A(t)$, where t is the time delay between pump and probe pulses.

TA signals collected from clean, anodized metal substrates reflect contributions from metal-oxide nanotubes, a thin oxide barrier layer at the substrate surface, and transient reflectivity of the substrate. To isolate nanotube contributions to TA, measurements were also performed on clean, unanodized substrates under the handling conditions (unannealed *versus* annealed) and using the same pump wavelengths. Substrate signals were then scaled as follows. Transient absorption signals for each anodized sample were summed over all probe wavelengths 700–907 nm, where induced absorption ($\Delta A > 0$) was observed, ignoring wavelengths with negative ΔA as no steady-state absorbance was seen at these wavelengths (Figure 6a). Signals from the corresponding unanodized substrates were summed over the same wavelengths. Dynamics

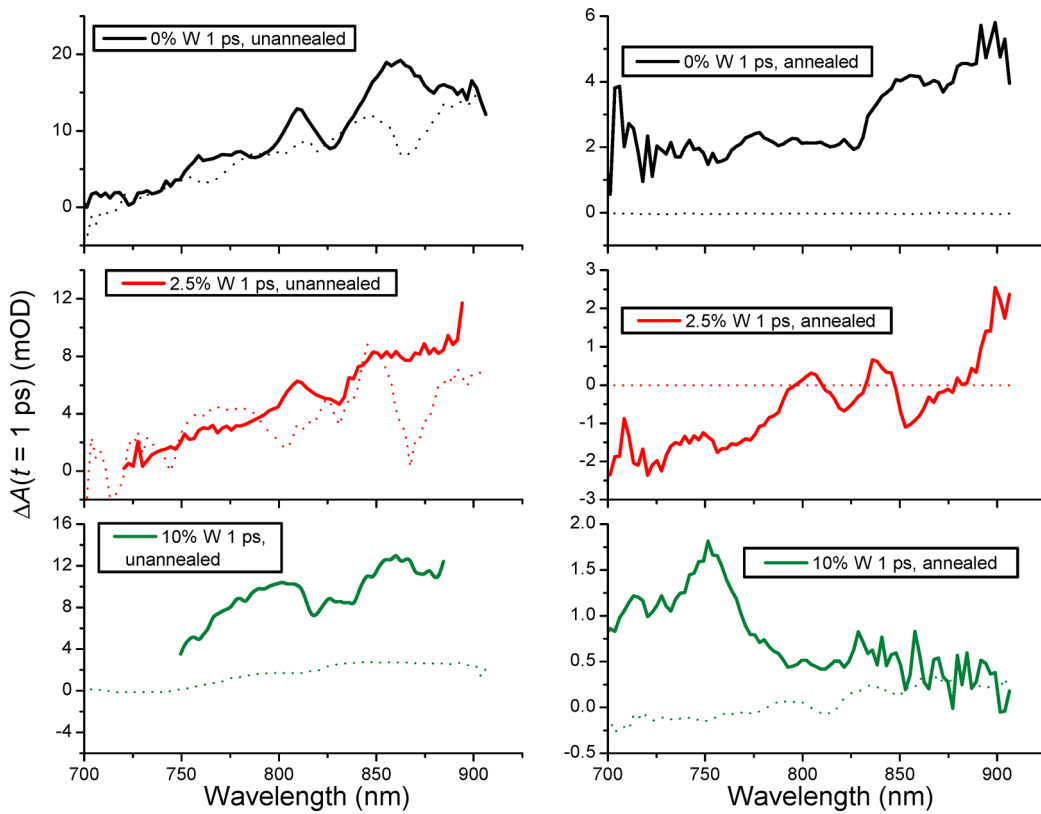


Figure 6. UV (340 nm) pump TA spectra at 1 ps pump–probe delay for nanotubes made from Ta alloys with W compositions of 0% (black, top row), 2.5% (red, middle row), and 10% (green, bottom row). Both unannealed (left column) and annealed (right column) nanotubes are shown. Dotted lines show transient spectra from clean, unanodized substrate under the same conditions (TA pump wavelength and annealing).

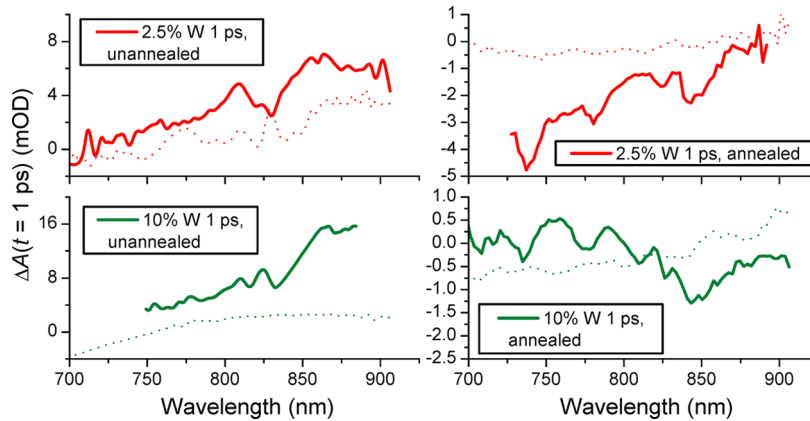


Figure 7. Visible (490 nm) pump TA spectra at 1 ps pump–probe delay for nanotubes made from Ta alloys with W compositions of 2.5% (red, top row) and 10% (green, bottom row). Both unannealed (left column) and annealed (right column) nanotubes are shown. Dotted lines show transient spectra from clean, unanodized substrate under the same conditions (TA pump wavelength and annealing).

from each nanotube-containing sample were then fitted using

$$\Delta A(t) = a_1 e^{-t/\tau_1} + a_2 e^{-t/\tau_2} + a_s \Delta A_s(t) + c \quad (1)$$

where $\Delta A_s(t)$ is the signal from the substrate alone, a_s is a positive scaling factor for the substrate signal, a_1 and a_2 are amplitudes of exponential decays with corresponding time constants τ_1 and τ_2 , and c is a constant

offset. The average decay lifetime of the nanotube signal over an observation window of ~ 3 ns is then calculated as

$$\langle \tau \rangle = \frac{a_1 \tau_1 + a_2 \tau_2}{a_1 + a_2} \quad (2)$$

Values for fitting parameters are given in Table 1.

Figure 7 shows TA spectra measured using UV (340 nm) excitation, with substrate signals scaled by

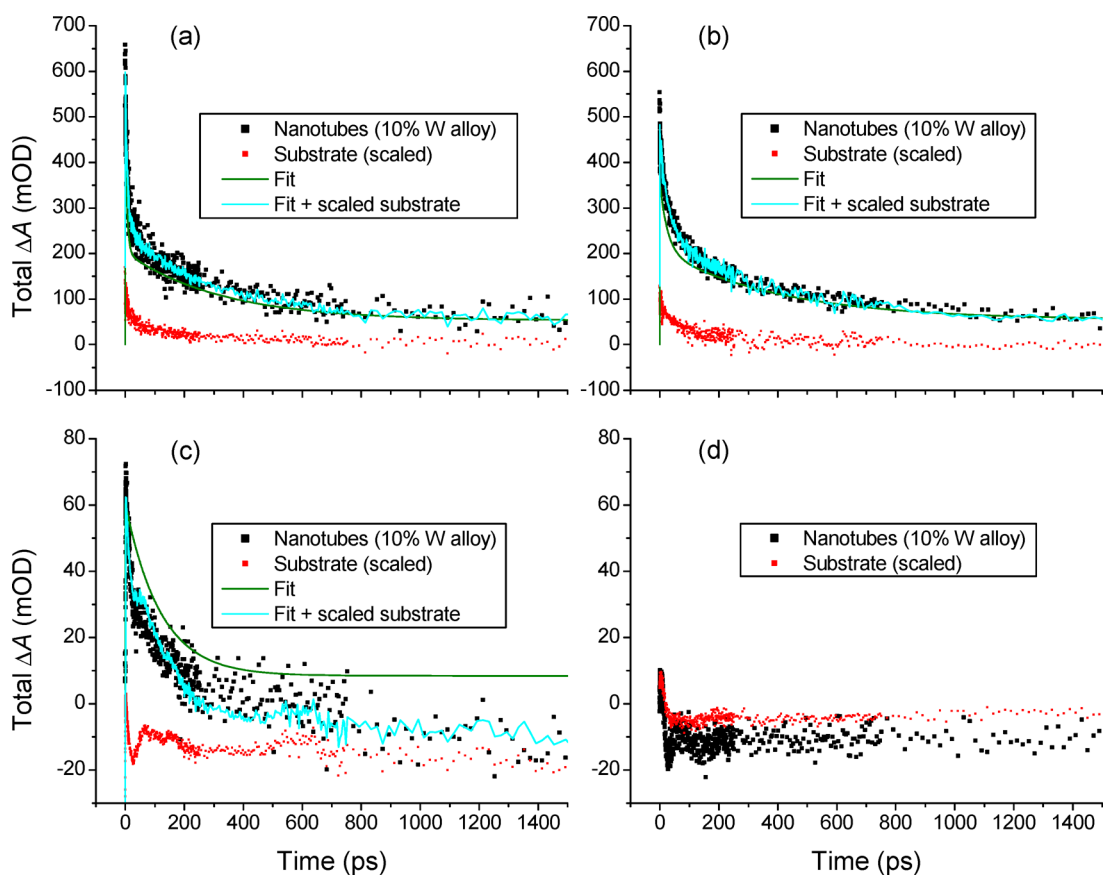


Figure 8. Transient absorption dynamics from nanotubes made by anodizing Ta alloy with 10% W content. Pump energy is 800 nJ/pulse, and signals are summed over probe wavelengths 700–907 nm where induced absorption ($\Delta A > 0$) is observed. (a) Unannealed sample, 340 nm pump; (b) unannealed sample, 490 nm pump; (c) annealed sample, 340 nm pump; (d) annealed sample, 490 nm pump. Background signals are measured from clean, unanodized substrates under the same conditions (pump wavelength and annealing), multiplied by a scaling factor, and incorporated into fits of the dynamics (see text). For (d), no fit is shown as the nanotubes do not show induced absorption except for a positive spike at zero delay.

TABLE 1. Carrier Lifetimes as a Function of Composition and Pump Wavelength

% W	annealing	pump wavelength (nm)	a_1 (mOD)	τ_1 (ps)	a_2 (mOD)	τ_2 (ps)	$\langle \tau \rangle$ (ps)	a_s
0	No	340	180 (50)	230 (40)			230 (40)	2.4 (0.1)
0	Yes	340	147 (6)	20 (2)			20 (2)	0.06 (0.07)
2.5	No	340	60 (10)	9 (3)			9 (3)	1.09 (0.01)
2.5	No	490	140 (40)	100 (30)			100 (30)	0.4 (0.1)
2.5	Yes	340	12.3 (0.8)	16 (2)			16 (2)	0 (0.01)
2.5	Yes	490	No signal from nanotubes					
10	No	340	240 (60)	6 (1)	150 (50)	300 (200)	130 (30)	0.4 (0.4)
10	No	490	150 (60)	25 (6)	150 (40)	400 (100)	220 (50)	0.5 (0.4)
10	Yes	340	52.0 (0.8)	120 (60)			120 (60)	0.2 (0.1)
10	Yes	490	No signal from nanotubes					

^a Values in parentheses are uncertainties in the fits. mOD = millioptical density units.

a_s . Spectra for doped samples excited with visible (490 nm) light are shown in Figure 8, with the pump light exciting W-doped Ta_2O_5 domains exhibiting a lower band gap. The spectra are shown at a pump–probe delay of 1 ps; analogous spectra at negative delays (probe arriving 1 ps before pump) are shown in Figures S3 and S4. In the red-to-near-IR region (700–907 nm), the nanotubes show positive ΔA consistent with absorption by initially unoccupied states

within the band gap, which we interpret as trapped electrons below the conduction-band edge similar to other metal oxides such as TiO_2 ,²³ Fe_2O_3 ,²⁴ and ZnO .^{25,26} A comparison with spectra acquired at negative delays (Figures S3 and S4) rules out experimental artifacts as the dominant origin of this signal. Unannealed samples show significant densities of defect states, especially for 10% W alloy nanotubes. Note that the increased defect absorbance exists despite

the decrease in the nanotube length with doping. For annealed samples, the absorption by defects approaches zero in doped samples. This is consistent with the fact that annealing improves the metal-oxide lattice crystallinity, therefore decreasing the defect density. Although the experiment does not yield an exact density of trapped carriers, the reduction in absorbance does reflect decreases in the number of trapped carriers due to annealing. Note that the defect density remains significant in pure Ta_2O_5 nanotubes even after annealing (Figure 7). Note also that charge trapping is identified as the most significant limiting factor in designing efficient photoanodes in PEC systems.³¹ Eliminating trap states should minimize the charge trapping and hence improve the photocurrent. This can be considered the main reason behind the observed enhancement of the photocurrent for the $Ta-W-O$ photoanodes, besides the red shift in the absorption spectrum and the efficient charge separation due to the staggered band alignment between Ta_2O_5 and WO_3 .⁹

Figure 8 and Figures S5 and S6 (see Supporting Information) depict the TA dynamics for the different fabricated samples from which the carrier lifetimes are extracted according to eqs 1 and 2. Table 1 summarizes the lifetimes at two pump wavelengths, namely 340 and 490 nm. It can be inferred that the 340 nm signal is capable of exciting the electrons from the VB to the CB of $Ta-W-O$ system. On the other hand, the 490 nm can excite the electrons into trap states within the bandgap. Table 1 shows that at the low pumping wavelength (340 nm), the lifetimes for 2.5% W and 10% W are very close for both unannealed and annealed samples (9 vs 16 ps for unannealed and annealed 2.5% W, respectively, and 130 versus 120 ps for unannealed and annealed 2.5% W and 10% W, respectively). The close lifetimes together with the low pumping wavelength assert that these lifetimes can be attributed to thermalization processes, especially that thermalization is affected by the band structure of the material and not its crystallinity. Furthermore, the lifetime at 340 nm for 2.5% W is much less than its 10% W counterpart suggesting a denser band structure in case of 2.5% W compared to the 10% W case,²⁴ in agreement with our previous study.⁹

As a final remark, it might be argued that shallow defect states might assist the promotion of the photo-generated electrons to the conduction band by providing a transit state to the electrons generated by sub-bandgap photons. However, it was found that conduction-band electron lifetimes in TiO_2 devices are in the millisecond range as observed in dye-sensitized solar cells, 9 orders of magnitude slower than the lifetime in trap states, and thus, it is extremely unlikely that electrons in Ta or $Ta-W$ oxide nanotube defect states can contribute to current in a PEC system. The effects of annealing in reducing defect density should improve the conductivity of the nanotubes. The TA results are thus consistent with the greatly enhanced photocurrent produced by the nanotubes containing 10% W (Figure 5b).

CONCLUSION

In summary, vertically oriented $Ta-W-O$ nanotube array films were fabricated *via* a simple electrochemical anodization of $Ta-W$ alloy foils. The nanotube length, diameter, and thickness were found to depend on the anodization conditions, with the foil containing 10% W showing more sensitivity to anodization conditions. Increasing the W content resulted in an increase in the nanotube length due to the increased stresses in the crystal lattice upon incorporation of W atoms. XRD analysis showed an expansion of 2.9% and 3.8% in the crystal lattice upon the addition of 2.5% and 10% W, respectively. The extent of expansion decreases with increasing the annealing time. XPS analysis illustrates that charge transfer occurs from Ta and O atoms to W atoms, as confirmed by the tail in the absorption spectra of $Ta-W-O$ nanotubes. Finally, the photocurrent of the nanotubes made of $Ta-W$ films containing 10% W was increased by about 10-fold compared to pristine Ta_2O_5 owing to efficient charge carriers separation due to the staggered band alignment between Ta_2O_5 and WO_3 and the red shift of the absorption spectrum. Ultrafast transient absorption spectroscopy illustrates the elimination of trap states upon annealing $Ta-W-O$ nanotubes, hence minimizing the charge carrier trapping, leading to a large photocurrent, whereas the trap states exist in pristine Ta_2O_5 nanotubes even after annealing.

MATERIALS AND METHODS

Prior to anodization, pure Ta samples as well as 2.5% and 10% W $Ta-W$ alloys (Goodfellow, USA) were cleaned in acetone for 30 min followed by 30 min in deionized water in an ultrasonic bath. A two-electrode electrochemical cell was used for anodization with Ta and $Ta-W$ samples as the working electrode and Pt foil as the counter electrode. For the nonadhering nanotubes, the anodization was carried out in a solution of concentrated sulfuric acid (95–98%) and HF (48%) where the sulfuric acid molarity was kept at 16.4 M and HF molarity was swept from 0.51 to 1.17 M. The anodization voltage was varied between 10 and 25 V, and the anodization time was varied between 5 to 35 min. For the well-adhered nanotubes, the same H_2SO_4/HF

solution was used with a volumetric ratio of 9:1. The solution was magnetically stirred during anodization at a speed of 60 rpm and kept at room temperature where the electrode separation was approximately 1 cm. The anodization voltage was kept at 14.5 V, and the anodization time varied between 2 and 4 min. After anodization, the as-anodized samples were annealed in an air atmosphere for 4 or 9 h at 450 °C at a rate of 1 °C/min for both heating and cooling.

A Zeiss SEM Ultra 60 field emission scanning electron microscope (FESEM) with an In-Lens detector was used to study the morphology of the samples at a voltage between 5 and 10 kV. A Thermo Scientific K-alpha XPS spectrometer with an Al anode was used for the XPS measurements, with the spectra

charge-referenced to O 1s at 532 eV. The crystalline phases were detected and identified using Alpha-1 Panalytical XRD instrument with a Cu $\text{K}\alpha$ radiation at $\lambda = 1.540598 \text{ \AA}$ at a scan step (20) of 0.004°. A Shimadzu UV-3101PC UV-Vis-NIR spectrophotometer was used for the optical characterization of the films. The photoelectrochemical measurements were performed in a three-electrode electrochemical cell. In this configuration, the nanotube films were used as photoanodes, platinum foil as the counter electrode, and saturated Ag/AgCl as the reference electrode, immersed in 1.0 M KOH. The dark and illuminated currents were monitored using a scanning potentiostat (CH Instruments, CHI 760) at a scan rate of 10 mV/s. A 300 W ozone-free xenon lamp equipped with AM 1.5G filter was used to simulate sunlight at 100 mW/cm².

Conflict of Interest: The authors declare no competing financial interest.

Supporting Information Available: Additional SEM images, onset potential table as a function of W content and nanotube length, additional carrier dynamics figures. This material is available free of charge via the Internet at <http://pubs.acs.org>.

Acknowledgment. M.A.E. would like to acknowledge the financial support by the U.S. Department of Energy, Office of Basic Energy Sciences, Grant No. DE-FG02-97-ER-14799 and N.K.A. would like to acknowledge the support by The American University in Cairo, Grant No. SS-PHY-RII 013-R7.

REFERENCES AND NOTES

- Lewis, N. S. Powering the Planet. *MRS Bull.* **2007**, *32*, 808–820.
- Grimes, C. A.; Varghese, O. K.; Ranjan, S. *Light, Water, Hydrogen: The Solar Generation of Hydrogen by Water Photoelectrolysis*; Springer: New York, 2008.
- Allam, N. K.; Poncheri, A. J.; El-Sayed, M. A. Vertically Oriented Ti-Pd Mixed Oxynitride Nanotube Arrays for Enhanced Photoelectrochemical Water Splitting. *ACS Nano* **2011**, *5*, 5056–5066.
- Mor, G. K.; Prakasam, H. E.; Varghese, O. K.; Shankar, K.; Grimes, C. A. Vertically Oriented Ti-Fe-O Nanotube Array Films: Toward a Useful Material Architecture for Solar Spectrum Water Photoelectrolysis. *Nano Lett.* **2007**, *7*, 2356–2364.
- Allam, N. K.; Alamgir, F.; El-Sayed, M. A. Enhanced Photo-assisted Water Electrolysis Using Vertically Oriented Anodically Fabricated Ti–Nb–Zr–O Mixed Oxide Nanotube Arrays. *ACS Nano* **2010**, *4*, 5819–5826.
- Ko, J. W.; Ryu, W.-H.; Kim, I.-D.; Park, C. B. Bi-Functional RuO₂-Co₃O₄ Core-Shell Nanofibers as a Multi-Component One-Dimensional Water Oxidation Catalyst. *Chem. Commun.* **2013**, *49*, 9725–9727.
- Allam, N. K.; Deyab, N. M.; Abdel Ghany, N. Ternary Ti-Mo-Ni Mixed Oxide Nanotube Arrays as Photoanode Materials for Efficient Solar Hydrogen Production. *Phys. Chem. Chem. Phys.* **2013**, *15*, 12274–12282.
- Allam, N. K.; Shaheen, B. S.; Hafez, A. M. Layered Tantalum Oxynitride Nanorod Array Carpets for Efficient Photoelectrochemical Conversion of Solar Energy: Experimental and DFT Insights. *ACS Appl. Mater. Interfaces* **2014**, *6*, 4609–4615.
- Nashed, R.; Alamgir, F. M.; Jang, S. S.; Ismail, Y.; El-Sayed, M. A.; Allam, N. K. Bandgap Bowing in Ta-W-O System for Efficient Solar Energy Conversion: Insights from Density-Functional Theory and X-Ray Diffraction. *Appl. Phys. Lett.* **2013**, *103*, 133905.
- Shimizu, K.; Kobayashi, K.; Thompson, G. E.; Skeldon, P.; Wood, G. C. The Migration of Fluoride Ions in Growing Anodic Oxide Films on Tantalum. *J. Electrochem. Soc.* **1997**, *144*, 418–423.
- Allam, N. K.; Feng, X. J.; Grimes, C. A. Self-Assembled Fabrication of Vertically Oriented Ta₂O₅ Nanotube Arrays, and Membranes Thereof, by One-Step Tantalum Anodization. *Chem. Mater.* **2008**, *20*, 6477–6481.
- Nashed, R.; Alamgir, F. M.; Jang, S. S.; Ismail, Y.; El-Sayed, M. A.; Allam, N. K. Towards a Perfect System for Solar Hydrogen Production: An Example of Synergy on the Atomic Scale. *Proc. SPIE* **2013**, *8822*, No. 88220A.
- Ho, S. F.; Contarini, S.; Rabalais, J. W. Ion-Beam-Induced Chemical Changes in the Oxyanions (Moyn-) and Oxides (Mox) where M = Chromium, Molybdenum, Tungsten, Vanadium, Niobium and Tantalum. *J. Phys. Chem.* **1987**, *91*, 4779–4788.
- Thomas, J. H.; Hammer, L. H. A Photoelectron Spectroscopy Study of CF₄/H₂ Reactive Ion Etching Residue on Tantalum Disilicide. *J. Electrochem. Soc.* **1989**, *136*, 2004–2010.
- Colton, R. J.; Guzman, A. M.; Rabalais, J. W. Electrochromism in Some Thin-Film Transition-Metal Oxides Characterized by X-Ray Electron Spectroscopy. *J. Appl. Phys.* **1978**, *49*, 409–416.
- Kerkhof, F. P. J. M.; Moulijn, J. A.; Heeres, A. The XPS Spectra of the Metathesis Catalyst Tungsten Oxide on Silica Gel. *J. Electron Spectrosc. Relat. Phenom.* **1978**, *14*, 453–466.
- Kurnia, F.; Hadiyawarman; Jung, C. U.; Jung, R.; Liu, C. Composition Dependence of Unipolar Resistance Switching in Ta_x Thin Films. *Phys. Status Solidi* **2011**, *5*, 253–255.
- Khyzhun, O. Y. XPS, XES and XAS Studies of the Electronic Structure of Tungsten Oxides. *J. Alloys Compd.* **2000**, *305*, 1–6.
- Nashed, R.; Hassan, W. M. I.; Ismail, Y.; Allam, N. K. Unraveling the Interplay of Crystal Structure and Electronic Band Structure of Tantalum Oxide (Ta₂O₅). *Phys. Chem. Chem. Phys.* **2013**, *15*, 1352–1357.
- Wu, Y.-N.; Li, L.; Cheng, H.-P. First-Principles Studies of Ta₂O₅ Polymorphs. *Phys. Rev. B* **2011**, *83*, 144105.
- Nozik, A. J. Photoelectrochemistry: Applications to Solar Energy Conversion. *Annu. Rev. Phys. Chem.* **1978**, *29*, 189–222.
- Yacobi, B. G. *Semiconductor Materials: An Introduction to Basic Principles*; Kluwer Academic/Plenum Publishers: New York, 2003.
- Tamaki, Y.; Hara, K.; Katoh, R.; Tachiya, M.; Furube, A. Femtosecond Visible-to-IR Spectroscopy of TiO₂ Nanocrystalline Films: Elucidation of the Electron Mobility before Deep Trapping. *J. Phys. Chem. C* **2009**, *113*, 11741–11746.
- Wheeler, D. A.; Wang, G. M.; Ling, Y. C.; Li, Y.; Zhang, J. Z. Nanostructured Hematite: Synthesis, Characterization, Charge Carrier Dynamics, and Photoelectrochemical Properties. *Energy Environ. Sci.* **2012**, *5*, 6682–6702.
- Li, M. J.; Xing, G. C.; Xing, G. Z.; Wu, B.; Wu, T.; Zhang, X. H.; Sun, T. C. Origin of Green Emission and Charge Trapping Dynamics in ZnO Nanowires. *Phys. Rev. B* **2013**, *87*, 115309.
- Bauer, C.; Boschloo, G.; Mukhtar, E.; Hagfeldt, A. Ultrafast Relaxation Dynamics of Charge Carriers Relaxation in ZnO Nanocrystalline Thin Films. *Chem. Phys. Lett.* **2004**, *387*, 176–181.
- Planells, M.; Pelleja, L.; Clifford, J. N.; Pastore, M.; De Angelis, F.; Lopez, N.; Marder, S. R.; Palomares, E. Energy Levels, Charge Injection, Charge Recombination and Dye Regeneration Dynamics for Donor-Acceptor pi-Conjugated Organic Dyes in Mesoscopic TiO₂ Sensitized Solar Cells. *Energy Environ. Sci.* **2011**, *4*, 1820–1829.
- Mohammadpour, R.; Zad, A. I.; Hagfeldt, A.; Boschloo, G. Comparison of Trap-State Distribution and Carrier Transport in Nanotubular and Nanoparticulate TiO₂ Electrodes for Dye-Sensitized Solar Cells. *ChemPhysChem* **2010**, *11*, 2140–2145.
- Listorti, A.; O'Regan, B.; Durrant, J. R. Electron Transfer Dynamics in Dye-Sensitized Solar Cells. *Chem. Mater.* **2011**, *23*, 3381–3399.
- Pendlebury, S. R.; Barroso, M.; Cowan, A. J.; Sivila, K.; Tang, J.; Graetzel, M.; Klug, D.; Durrant, J. R. Dynamics of Photo-generated Holes in Nanocrystalline Alpha-Fe₂O₃ Electrodes for Water Oxidation Probed by Transient Absorption Spectroscopy. *Chem. Commun.* **2011**, *47*, 716–718.
- Tang, J. W.; Durrant, J. R.; Klug, D. R. Mechanism of Photocatalytic Water Splitting in TiO₂: Reaction of Water with Photoholes, Importance of Charge Carrier Dynamics, and Evidence for Four-Hole Chemistry. *J. Am. Chem. Soc.* **2008**, *130*, 13885–13891.